

A Full Geometric and Photometric Calibration Method for Oblique-viewing Endoscope

C. Wu* ⁺, B. Jaramaz, PhD* ^{**}, S.G. Narasimhan, PhD*

chenyuwu@cmu.edu, branko@icaos.org, srinivas@cs.cmu.edu

* Robotics Institute, School of Computer Science

Carnegie Mellon University, 5000 Forbes Avenue, Pittsburgh, PA 15213

** Institute for Computer Assisted Orthopaedic Surgery, The Western Pennsylvania Hospital Mellon Pavilion

Suite 242, 4815 Liberty Avenue, Pittsburgh, PA 15224

⁺ Correspondence: Chenyu Wu, 201 Smith Hall, CMU, 5000 Forbes Avenue, Pittsburgh, PA 15213

Abstract

Oblique-viewing endoscopes (oblique scope) are widely used in computer assisted surgeries. Viewing direction of an oblique scope can be changed by rotating the scope cylinder, which extends the field of view, but makes the scope geometric calibration process more difficult. Although few methods have yet been developed, the calibration is critical for applying augmented reality technologies such as stereo to oblique scope related procedures. Moreover, based on our knowledge, no photometric calibration method has been introduced to endoscope, which is however important for illumination based visualization techniques e.g. shape from shading. In this paper, we present a complete calibration process for oblique-viewing endoscope to estimating both geometric and photometric properties. Experimental results demonstrate that our methods is practical and accurate.

Keywords: Calibration, Oblique-viewing Endoscope, Geometric, Photometric

Introduction

One of the main goals of computer assisted orthopedic surgery is to enable true minimally invasive surgery (MIS). As a key MIS tool, endoscope is attracting increasing attention for its potential role in computer assisted surgery, especially in the surgical navigation system. By tracking the endoscope in space using a position localizer, its role can be significantly augmented. For example, it can be used to create MIS augmented reality systems, to merge the virtual and real endoscopic images [1], to overlay real endoscopic images with 3D surfaces derived from CT images [2], or to recover the 3D shape from a single endoscopic image [3, 4] or multiple images [5, 6, 7].

Camera geometric calibration, as an important step in endoscope related applications, mostly based on Tsai's model [8], has been addressed in several work [2, 9, 10, 11]. However, except [11], most of these methods deal with the forward-viewing endoscope, in which the viewing direction is aligned with the axis of the endoscope. Due to the constraints of the small incision, the range of the movement of such a tool is restricted thus the field of view is very small. In order to view sideways, oblique scope has been designed to have a tilted viewing direction, and a wider viewing field could be reached by rotating the scope cylinder. Fig. 1 illustrates an oblique-viewing endoscope. Rotation happens between the scope cylinder and the camera head. Yamaguchi et al. first modelled and calibrated the oblique scope [11, 12]. They formulate the rotation parameter of the scope cylinder as another external parameters in Tsai's camera model. They use two extra transformations to compensate the rotation θ of the lens system and still of the camera head. Yamaguchi et al's camera model successfully compensates the rotation effect but their method requires five additional parameters and the model is complicated. In this work we propose an alternative approach to simplify the calibration. We attach an optical marker to the scope cylinder instead of the camera head, with a newly designed coupler (as Fig. 1(b) illustrates). As a result our camera model is simpler and we only need to estimate one additional parameter.

Camera photometric calibration, another important process in illumination related applications, is performed to find the relationship between the image irradiance and image intensity for the camera. This relationship is called the camera response function. Traditional photometric calibration recovers only the camera response function by changing the camera's exposure time. Compared with regular cameras, it is hard to control the exposure time for endoscope, and the light spacial distribution can be anisotropy. Therefore we develop a method to calibrate all these unknown parameters simultaneously.

Geometric Calibration

Common orthopedic endoscope has a single camera and one or more point light sources equipped at the tip of the scope. For this work, we use two oblique endoscopes as examples. One of them is shown in Fig. 1 and another one is in Fig. 6.

Model for Oblique-viewing Endoscope

Yamaguchi et al's camera model is based on Tsai's model [8, 9]:

$$\begin{aligned}\lambda p_i &= A \cdot {}^cT_m(\theta) \cdot {}^mT_w \cdot P_w \\ {}^cT_m(\theta) &= T_R(-\theta; l_h(\theta))T_R(\theta; l_s){}^cT_m(0)\end{aligned}\quad (1)$$

where P_w is a 3D point in the world coordinates, p_i is the corresponding 2D image pixel. mT_w is a rigid transformation from the world coordinates to the optical marker coordinates, ${}^cT_m(\theta)$ is a rigid transformation from the marker (camera head) to the camera coordinates. ${}^cT_m(\theta)$ is dependent on the rotation angle θ . By considering the marker coordinates (camera head) as a reference, only the lens system rotates while the camera head, i.e., the image plane, remains fixed irrespective of the rotation. Yamaguchi et al. [11, 12] describe such a transformation due to the rotation by decomposing the one physical rotation into two mathematical rotations. $T_R(\theta; l_s)$ is a rotation of both scope cylinder and the camera head (image plane) around the axis of cylinder l_s . $T_R(-\theta; l_h(\theta))$ is an inverse rotation of the image plane around the z-axis of lens system l_h . Both l_s and l_h have two unknown parameters. Although this model works well, it is very complicated.

Fig. 2 (a) shows the modified geometric model from that of Yamaguchi et al. by attaching an optical marker on the scope cylinder instead of the camera head.

$$\begin{aligned}\lambda p'_i &= A \cdot {}^cT_m \cdot {}^mT_w \cdot P_w \\ p_i &= R(\theta) \cdot (p'_i - cc) + cc\end{aligned}\quad (2)$$

where P_w is a 3D point in the world coordinates, p'_i is the corresponding 2D image pixel without rotation, p_i is the image pixel with rotation θ . mT_w is a rigid transformation from world coordinates to the optical marker coordinates, cT_m is a rigid transformation from the marker (scope cylinder) to the camera coordinates and independent on θ . cc is the principal point which is an intrinsic parameter. $R(\theta)$ represents a rotation of the image plane around cc by θ . Thus camera intrinsic matrix A and external matrix cT_m can be calibrated by using Zhang's method [9] and mT_w can be obtained directly from the tracking system. In our model we only need to estimate the rotation angle.

Rotation angle can be estimated by using a rotary encoder, as Yamaguchi et al [12] did. When it is absent, the rotation angle can be estimated by using two optical markers: one attached to the scope cylinder and the other one on the rod (camera head).

A comparison between our model and Yamaguchi et al's model is listed in Fig. 3. Yamaguchi et al's use the camera head as a reference coordinates in their hand-eye calibration system. Since surgeons rotate the scope cylinder with respect to the camera head in order to view sideways, it is a natural way to consider the camera head as a reference. However it makes the camera model very complex. To think in an opposite way, no matter how surgeons rotate the scope cylinder, if the reference coordinates is on the cylinder, the lens system is fixed with respect to the cylinder but the camera head rotates around θ . Thus the external parameters are not affected by the rotation anymore. Since the image plane is in the camera head, the rotation only affects the image plane. Our method is therefore developed based on above observations. Yamaguchi et al's model needs five more parameters but we only need one. They use two optical markers and one rotary encoder. We only need two optical markers.

Estimate Rotation Angle Using Two Optical Markers

Let the marker attached to the scope cylinder be Marker 1 and the marker to the rod (camera head) be Marker 2 (Fig. 3 (b)). As Fig. 4 shows, when we rotate the camera head around the scope cylinder by θ , point P_r in Marker 2's coordinates O_2 will move along a circle with respect to a point O on the axis of the scope cylinder, in Marker 1's coordinates O_1 . Thus we can estimate the center O of the circle first and compute θ as:

$$\theta = \arccos \frac{\|\vec{OP}_r^A\|^2 + \|\vec{OP}_r^B\|^2 - \|\vec{P}_r^A \vec{P}_r^B\|^2}{2\|\vec{OP}_r^A\| \cdot \|\vec{OP}_r^B\|} \quad (3)$$

A is the position of O_2 when $\theta = 0$ and B is the position of O_2 given a rotation θ . The center of the circle can be represented in terms of the transformation from the world coordinates O_w to Marker 1's coordinates O_1 and Marker 2's coordinates O_2 , and at least 3 different positions of Marker 2 (O_2) (with different θ) are necessary.

Estimation of the center of circle in 3D

We rotate the camera head around the cylinder to acquire 3 different positions of Marker 2. Let the transformation matrix from the world coordinates O_w to both Marker 1's coordinates O_1 and Marker 2's coordinates O_2 for position i be $({}^{o_1}T_{o_w}^i, {}^{o_2}T_{o_w}^i)$ ($i = 1, 2, 3$). Given any point \vec{P}_r in O_2 , we first compute the position \vec{P}_i in O_1 corresponding to different rotations as:

$$\vec{P}_i = {}^{o_1}T_{o_w}^i \cdot ({}^{o_2}T_{o_w}^i)^T \cdot \vec{P}_r, i = 1, 2, 3. \quad (4)$$

Therefore, O is the center of the circumcircle of the triangle $(\vec{P}_1, \vec{P}_2$ and $\vec{P}_3)$.

Let $\vec{R}_1 = \vec{P}_1 - \vec{P}_3$, $\vec{R}_2 = \vec{P}_2 - \vec{P}_3$, the normal of the triangle is $\vec{n} = \vec{R}_1 \times \vec{R}_2$. The perpendicular bisector \vec{L}_1 of \vec{R}_1 and \vec{L}_2 of \vec{R}_2 can be computed as:

$$\begin{aligned} \vec{L}_1 &= \vec{P}_3 + \vec{R}_1/2 + \lambda_1 \cdot \vec{n} \times \vec{R}_1 \\ \vec{L}_2 &= \vec{P}_3 + \vec{R}_2/2 + \lambda_2 \cdot \vec{n} \times \vec{R}_2 \end{aligned} \quad (5)$$

where λ_1 and λ_2 are parameters of the line \vec{L}_1 and \vec{L}_2 . The intersection of these two lines are the center of the circle. From Equation 5 we can derive the center of the circle as:

$$\vec{O} = \frac{(\vec{R}_2 - \vec{R}_1) \cdot \vec{R}_1/2}{|\vec{R}_1 \times \vec{R}_2|^2} \cdot (\vec{R}_1 \times \vec{R}_2) \times \vec{R}_2 + \vec{R}_2/2 + \vec{P}_3 \quad (6)$$

It can be easily proved that O does not depend on the selection of \vec{P}_r . Since at least 3 different positions are necessary, we rotate the camera head around the scope cylinder by N different angles.

We then apply a RANSAC algorithm to estimate \vec{O} using random positions, and select \vec{O} which corresponds to the smallest variance as the center of the circle. The pseudo code of RANSAC is listed in Table 1. It can be also proved that θ does not depend on the selection of P_r either. A

Table 1: Pseudo code of RANSAC for estimating the center of the circle

```

Loop k=1:K (K=2000)
  Generate a random point  $P_r$  from 3D space
  Generate random number  $x, y, z$  between  $[1, N]$ 
  Compute  $P_x, P_y, P_z$  using Eq. 4
  Compute  $O_k$  using Eq. 6
  Compute  $|O_k P_j|, j \in [1, N], j \neq x, y, z$ 
  Compute  $v_k$ 
  Save  $O_k, v_k$ 
End loop
Return  $O_q, q = \arg \min(v_k)$ 

```

Table 2: Pseudo code of RANSAC for estimating the rotation angle

```

Loop k=1:K (K=1000)
  Generate a random point  $P_r$  from 3D space
  Compute  $P_A$  and  $P_B$  using Eq. 4
  Compute  $\theta_k$  using Eq. 3
End loop
Return  $\theta = \frac{1}{K} \sum_k \theta_k$ 

```

similar RANSAC algorithm as Table 2 shows is then used to compute θ . Fig. 5 shows the estimated rotation angle using RANSAC algorithm for two different endoscopes. The red curves are output angles from different RANSAC iterations, the black curve is the average angle. We can see the variance of the estimation is very small (less than 0.2 degree).

Experimental Results

We tested our algorithm using two different systems. We first tested it in our lab. We used Stryker 344-71 arthroscope Vista (70 degree, 4mm) oblique-viewing endoscope, DYONICS DyoCamTM 750 video camera, DYONICS DYOBRITE 3000 light source, Polaris (Northern Digital Inc., Ontario, Canada) optical tracker. Next we tested it in conjunction with our standard operating room equipment. We used Smith & Nephew video arthroscope - autoclavable SN-OH 272589 (30 degree, 4mm), DYONICS video camera and light source, OPTOTRAK (Northern Digital Inc., Ontario, Canada) optical tracker. Fig. 6 shows the different endoscopes and optical trackers.

The endoscope was first fixed and the calibration pattern was rotated on the table for capturing images. A set of images were captured without a rotation between the scope cylinder and camera head. They were used to estimate both the intrinsic matrix A (including focal length and radial distortion coefficients) and extrinsic matrix cT_m using Zhang's method [9] (implemented using

OpenCV functions). After that, when there was a rotation happening between the camera head and the scope cylinder, another set of images were captured and the center of the circle can be computed by using Eq. 6. Next, we fixed the calibration pattern, with two optical markers attached to the scope cylinder and the camera head, we captured a set of images by applying general motions of the endoscope (moving the whole scope body or rotating the camera head with respect to the scope cylinder (or more natural description: rotating the scope cylinder with respect to the camera head)). This set of images were used to estimate the rotation angles. The initial position of the camera head was considered as the reference position A illustrated in Fig. 4. Fig. 7 illustrates the back projection of 3D corners of the calibration pattern with (blue) and without (red) a rotation compensation. Green points are ground truth. For each rotation angle of the endoscope, we computed the average back projection error for this angle as:

$$\epsilon(\theta) = \frac{1}{M} \sum_{i=1}^M |p_i - p(P_i, \theta)| \quad (7)$$

where P_i is a 3D point in the world coordinates, p_i is the corresponding 2D image pixel, $p(P_i, \theta)$ is the back projected 2D image pixel of P_i . M is the number of corners on the calibration pattern. We have used different grid patterns (3x4 as shown in Fig. 7, 4x5 and 5x6. The size of each checker is 2mm x 2mm). In order to obtain enough light on the grid pattern, the endoscope needs to be placed very close to the target (usually 5-15mm). So the smaller grid cannot capture the radial distortion but the bigger grid will exceed the field of view. The 5x6 grid gave the best results.

Finally we did many trials by moving and rotating the endoscope randomly and estimate θ simultaneously. The average back projection error with respect to the different rotation angles are shown in Fig. 8. Fig. 8 (a) is the result using Stryker 344-71 arthroscope Vista (70 degree, 4mm) and Polaris optical tracker. Fig. 8 (b) is the result using Smith & Nephew video arthroscope - autoclavable SN-OH 272589 (30 degree, 4mm) and OPTOTRAK optical tracker. The red curve represents the back projection error without taking into account of the rotation angle, and the blue curve shows the error with considering the rotation angle. The results show that including the rotation angle into the camera model significantly improve the accuracy of the calibration.

Fig. 8 shows that different endoscopes have different accuracy. The reason is that endoscopes have different magnification and optical trackers have different accuracy (according to the manufacturer, RMS error is 0.1mm for OPTOTRAK and 0.3mm for Polaris). Yamaguchi et al. [11, 12] used an OTV-S5C laparoscope (Olympus Optical Co. Ltd., Tokyo, Japan) and Polaris optical tracker. They have achieved a high accuracy of less than 5mm back projection error when the rotation angle is within 140 degrees. Our results show that we can achieve the same level accuracy when the rotation angle is within 75 degrees. Beyond this range, due to the bigger magnification, larger radial distortion and poorer lighting (a comparison between images used in our experiment and Yamaguchi et al.'s experiment is shown in Fig. 7), the back projection error is increased to 13mm when the rotation angle is 100 degrees. When given the same quality endoscopes, we should be able to achieve the same level of accuracy.

Photometric Calibration

Based on our knowledge, photometric calibration for the endoscope has not been studied in the literature. In this paper we propose a method to compute the camera response function, light source intensity and light spacial distribution function, simultaneously, inspired by [13].

Reflectance Model under Near-field Lighting and Projective Projection

Assume the bone surface is Lambertian, the scene radiance can be computed according to Lambertian cosine law as:

$$R(x, y, z) = G_0 \rho \left(\frac{\mathbf{n} \cdot \mathbf{l}_1}{r_1^2} + \frac{\mathbf{n} \cdot \mathbf{l}_2}{r_2^2} \right) \quad (8)$$

where G_0 is the intensity of two light sources s_1 and s_2 , ρ is the surface albedo, \mathbf{n} is the surface normal, \mathbf{l}_1 and \mathbf{l}_2 are two light rays arriving at the surface, and r_1 and r_2 are the distances from each light source to the surface. (x, y, z) indicates the 3D location of the scene point P (see Fig. 9).

On the other hand, the image irradiance E can be estimated from the image intensity v given the camera response function $H(\cdot)$:

$$E(x, y) = \frac{H^{-1}(v(x, y))}{M(x, y)} \quad (9)$$

where, $M(x, y)$ is the spatial distribution of the source intensity that is assumed to be equal for both light sources. Assume there is no loss of the energy when light rays propagate from the scene to the camera lens, so the radiance remains the same and thus $R = E$. Combine Eq. 8 and 9 we have:

$$\begin{aligned} H^{-1}[v(x, y)] &= \rho \cdot G_0 \cdot \tilde{M}(x, y) \\ \tilde{M}(x, y) &= M(x, y) \cdot \left(\frac{\mathbf{n} \cdot \mathbf{l}_1}{r_1^2} + \frac{\mathbf{n} \cdot \mathbf{l}_2}{r_2^2} \right) \end{aligned} \quad (10)$$

For calibration, we use a Macbeth color chart with known albedo for each patch. We capture a set of images by varying light source intensity for each patch. We apply log to both sides of Eq. 10 to obtain a linear system of equations:

$$h[v_i^j(x, y)] = p_i + g_j + \tilde{m}(x, y) \quad (11)$$

where i indicates the different albedos and j indexes the light intensity. $h[v_i^j(x, y)] = \log\{H^{-1}[v_i^j(x, y)]\}$, $p_i = \log(\rho_i)$, $g_j = \log(E_{0j})$ and $\tilde{m}(x, y) = \log[\tilde{M}(x, y)]$. The unknowns ($h(\cdot)$, g_j , $\tilde{m}(x, y)$) can be obtained by solving this linear system of equations. The term $M(x, y)$ is then estimated from $\tilde{M}(x, y)$ by measuring the distance to the chart from the scope tip. An image of a square patch with uniform albedo is captured and distortion is then removed. We measure the distance between the scope tip and four corners, and then compute the term $\frac{(n) \cdot \mathbf{l}_1}{r_1^2} + \frac{(n) \cdot \mathbf{l}_2}{r_2^2}$ for each image pixel. Finally $M(x, y)$ is estimated by removing the above term from $\tilde{m}(x, y)$.

Solution to $h(\cdot)$

Given the same light intensity g_j and pixel value $v(x, y)$ but two different albedos ρ_{i_1} and ρ_{i_2} , we have

$$\begin{cases} h[v_{i_1}^j(x, y)] - g_j - \tilde{m}(x, y) - p_{i_1} = 0 \\ h[v_{i_2}^j(x, y)] - g_j - \tilde{m}(x, y) - p_{i_2} = 0 \end{cases} \quad (12)$$

Subtract the first line from the second line of Eq. 12 we obtain:

$$h[v_{i_2}^j(x, y)] - h[v_{i_1}^j(x, y)] = p_{i_2} - p_{i_1} \quad (13)$$

We use different pixels in the same image (albedo) or different images (albedos) to make as many equations as Eq. 13, as long as we fix the light intensity for each pair of albedos. Since $v_{i_1}^j(x, y)$ changes from 0 to 255(image intensity), we only need 256 such equations and stack them as:

$$\begin{bmatrix} \dots & 1^* & -1^* & \dots \\ \dots & -1^\# & 1^\# & \dots \\ & \dots & & \dots \end{bmatrix} \cdot \begin{bmatrix} h(0) \\ h(1) \\ \vdots \\ h(255) \end{bmatrix} = \begin{bmatrix} p_{i_2} - p_{i_1} \\ p_{i_4} - p_{i_3} \\ \vdots \end{bmatrix} \quad (14)$$

where 1^* and -1^* correspond to the column $v_{i_2}^j(x, y) + 1$ and $v_{i_1}^j(x, y) + 1$, respectively. $1^\#$ and $-1^\#$ correspond to the column $v_{i_4}^j(x, y) + 1$ and $v_{i_3}^j(x, y) + 1$, respectively. Therefore $h(v)$ is solved from Eq. 14 and $H(v) = \exp(h(v))$.

Solution to g_j

Given the same albedo p_i and pixel value $v(x, y)$ but two different light intensities g_{j_1} and g_{j_2} we have

$$\begin{cases} h[v_i^{j_1}(x, y)] - g_{j_1} - \tilde{m}(x, y) - p_i = 0 \\ h[v_i^{j_2}(x, y)] - g_{j_2} - \tilde{m}(x, y) - p_i = 0 \end{cases} \quad (15)$$

Subtract the first line from the second line of Eq. 15:

$$h[v_i^{j_2}(x, y)] - h[v_i^{j_1}(x, y)] = g_{j_2} - g_{j_1} \quad (16)$$

We use the minimum light intensity g_1 as a reference, for other light intensities $g_j, j = 2, \dots, N_{light}$, we have

$$g_j = g_1 + h[v_i^j(x, y)] - h[v_i^1(x, y)] \quad (17)$$

Given estimated $h(v(x, y))$ and by changing the albedos and pixels, we compute the average value for each g_j as follows and $\bar{G}_j = \exp(g_1) \cdot \exp(\bar{g}_j)$.

$$\bar{g}_j = g_1 + \frac{1}{N_{albedo}} \cdot \frac{1}{N_{pixels}} \sum_i \sum_{x,y} \{h[v_i^j(x, y)] - h[v_i^1(x, y)]\} \quad (18)$$

Solution to $\tilde{m}(x, y)$

Again, Given the same albedo p_i and light intensity g_j but two different pixels (x_p, y_p) and x_q, y_q we have

$$\begin{cases} h[v_i^j(x_p, y_p)] - g_j - \tilde{m}(x_p, y_p) - p_i = 0 \\ h[v_i^j(x_q, y_q)] - g_j - \tilde{m}(x_q, y_q) - p_i = 0 \end{cases} \quad (19)$$

Subtract the first line from the second line of Eq. 19:

$$h[v_i^j(x_p, y_p)] - h[v_i^j(x_q, y_q)] = \tilde{m}(x_p, y_p) - \tilde{m}(x_q, y_q) \quad (20)$$

For each g_j and ρ_i , instead of using $C_{N_{pixels}}^2$ different pairs of pixels, we choose only $N_{pixels} = 720 \times 480$ pairs and stack the equations like the following:

$$\underbrace{\begin{bmatrix} 1 & -1 & & & \\ & 1 & -1 & & \\ & & & \ddots & \\ & & & & \ddots \\ -1 & & & & 1 \end{bmatrix}}_A \cdot \begin{bmatrix} \tilde{m}(x_1, y_1) \\ \tilde{m}(x_2, y_2) \\ \vdots \\ \tilde{m}(x_{N_{pixels}}, y_{N_{pixels}}) \end{bmatrix} = \begin{bmatrix} h[v_i^j(x_1, y_1)] - h[v_i^j(x_2, y_2)] \\ h[v_i^j(x_2, y_2)] - h[v_i^j(x_3, y_3)] \\ \vdots \\ h[v_i^j(x_{N_{pixels}}, y_{N_{pixels}})] - h[v_i^j(x_1, y_1)] \end{bmatrix} \quad (21)$$

It's not practical to solve Eq. 21 using singular value decomposition (SVD) directly since matrix A requires a huge memory. However we notice that the matrix A in Eq. 21 is a special N_{pixels} by N_{pixels} matrix such that we could get the inverse directly by using Gauss-Jordan Elimination:

$$A^{-1} = \begin{bmatrix} 0 & & & & 0 & -1 \\ -1 & 0 & & & 0 & -1 \\ -1 & -1 & 0 & & 0 & -1 \\ \vdots & \vdots & \vdots & \cdots & 0 & -1 \\ -1 & -1 & -1 & \cdots & -1 & -1 \end{bmatrix} \quad (22)$$

Thus we successfully compute each element of $\tilde{m}(x, y)$ independently and again, $M(\tilde{x}, y) = \exp(\tilde{m})$.

Experimental Results

A series of images of color chart are used for photometric calibration. We use 6 different levels of image intensity. In Fig. 10, (a),(b) and (c) show the camera response function with Red, Green, Blue channels. (d) shows the recovered light intensity in different levels and compared to the ground truth. Smaller number in x-axis corresponds to higher intensity. We see a bit variance when light intensity is high, that can be caused by the saturation. (e) shows the original image and (f) shows \tilde{m} . (g) shows the cosine term $\frac{(n) \cdot l_1}{r_1^2} + \frac{(n) \cdot l_2}{r_2^2}$ and (h) shows the spacial distribution function $m(x, y)$.

Conclusions and Discussions

In this paper we have developed a full calibration process for both geometric and photometric properties of endoscopes. Our geometric calibration method simplified previous work by designing a coupler attached to the scope cylinder. It is easy to implement and practical to apply with the standard operating room equipments such as the navigation system. The only drawback of this method is the requirement of two markers to be visible to optical trackers all the time otherwise the method will fail.

According to our knowledge, photometric calibration has not been applied by others. Most of previous work did not rely on the physical model of endoscope light sources, or they restricted the changing of light sources during the operation. A few of recent work applied shape-from-shading to endoscopic images based on a simplified light source model without calibrating the model parameters. However, in order to reconstruct an accurate shape from endoscopic images, the knowledge of light sources is necessary and important.

Both geometrical and photometrical parameters are very useful for 3D visualization and reconstruction of anatomical structures such as bones. We have already applied the calibrated endoscopes to artificial spine reconstruction [14]. In that work, we reconstructed the spine from each individual endoscopic images based on a calibrated photometric model. With calibrated geometric parameters of the endoscope, we were able to transfer all individual reconstructed shapes to the world coordinates and thus find the global occluding boundaries, which helped the later re-grow of the shape-from-shading. The results demonstrate that using calibrated endoscopes can achieve very good reconstruction result which is promising for the real surgical applications.

References

- [1] Clarkson MJ, Rueckert D, King AP, Edwards PJ, Hill DLG, Hawkes DJ. Registration of video images to tomographic images by optimising mutual information using texture mapping. *Proc. of MICCAI 1999*;1679:579-588.
- [2] Dey D, Gobbi DG, Slomka PJ, Surry KJ, Peters TM. Automatic fusion of freehand endoscopic brain images to three-dimensional surfaces: creating stereoscopic panoramas. *IEEE Trans. on Medical Imaging* 2002;21(1):23-30.
- [3] Deguchi K, Okatani T. Shape reconstruction from an endoscope image by shape-from-shading technique for a point light source at the projection center. *Proc. of IEEE Computer Society Workshop on Mathematical Methods in Biomedical Image Analysis (MMBIA) 1996*. p 290-298.
- [4] Forster CHQ, Tozzi CL. Towards 3D reconstruction of endoscope images using shape from shading. *Proc. of XIII Brizilian Symposium on Computer Graphics and Image Processing* 2000. p 90-96.
- [5] Mourgues F, Coste-Manière E. Flexible calibration of actuated stereoscopic endoscope for overlay in robot assisted surgery. *Proc. of MICCAI 2002*. p 25-34.

- [6] Stoyanov D, Darzi A, Yang GZ. A practical approach towards accurate dense 3D depth recovery for robotic laparoscopic surgery. *Computer Aided Surgery* 2005;10(4):199-208.
- [7] Wengert C, Reeß M, Cattin PC, Székely G. Fully Automatic Endoscope Calibration for Intraoperative Use. *Bildverarbeitung für die Medizin*, Springer-Verlag 2006. p 419-423.
- [8] Tsai RY. A versatile camera calibration technique for high-accuracy 3D machine vision metrology using off-the-shelf TV cameras and lenses. *IEEE Journal of Robotics and Automation* 1987;RA-3:323-344.
- [9] Zhang Z. A flexible new technique for camera calibration. *Microsoft Research* 1998;MSR-TR-98-71.
- [10] Shahidi R, Bax MR, Maurer CR, Johnson JA, Wilkinson EP, Wang B, West JB, Citardi MJ, Manwaring KH, Khadem R. Implementation, calibration and accuracy testing of an image-enhanced endoscopy system. *IEEE Trans. on Medical Imaging* 2002;21(12):1524-1535.
- [11] Yamaguchi T, Nakamoto M, Sato Y, Nakajima Y, Konish K, Hashizume M, Nishii T, Sugano N, Yoshikawa N, Yonenobu K, Tamura S. Camera Model and Calibration Procedure for Oblique-Viewing Endoscope. *Proc. of MICCAI* 2003;2879:373-381.
- [12] Yamaguchi T, Nakamoto M, Sato Y, Konishi K, Hashizume M, Sugano N, Yoshikawa H, Tamura S. Development of a camera model and calibration procedure for oblique-viewing endoscopes. *Computer Aided Surgery* 2004;9(5):203-214.
- [13] Litvinov A, Schechner YY. Addressing radiometric nonidealities: a unified framework. *Proc. of Computer Vision and Pattern Recognition (CVPR)* 2005;2:52-59.
- [14] Wu C, Narasimhan S, Jaramaz B. A Multi-Image Shape-from-Shading Framework for Near-Lighting Perspective Endoscopes. *International Journal of Computer Vision (IJCV)*, February, 2009.

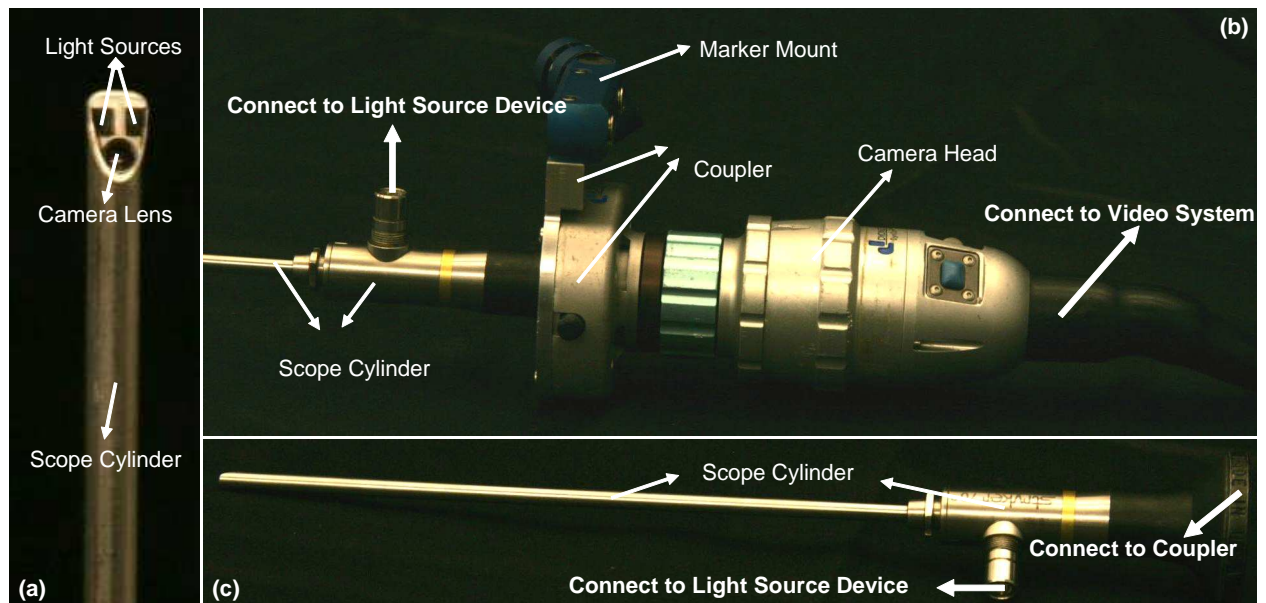


Figure 1: Stryker 344-71 arthroscope Vista (70 degree, 4mm): an oblique endoscope consists of a scope cylinder with a lens and point light sources at the tip (the tip has a tilt from the scope cylinder), a camera head that captures video images, and a light source device that supports the illumination. Scope cylinder is connected to the camera head via a coupler. This connection is flexible such that you can rotate either the scope cylinder or the camera head separately, or rotate them together.

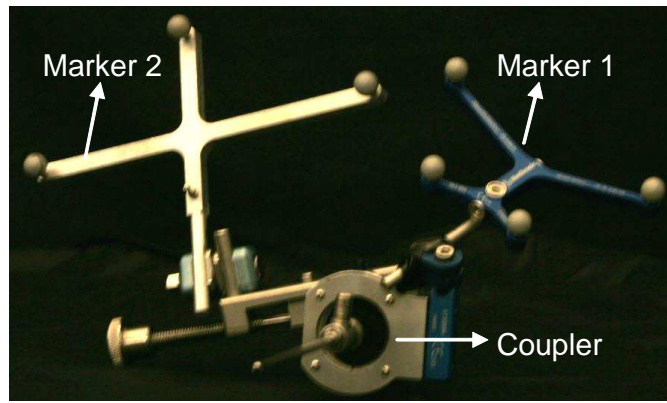
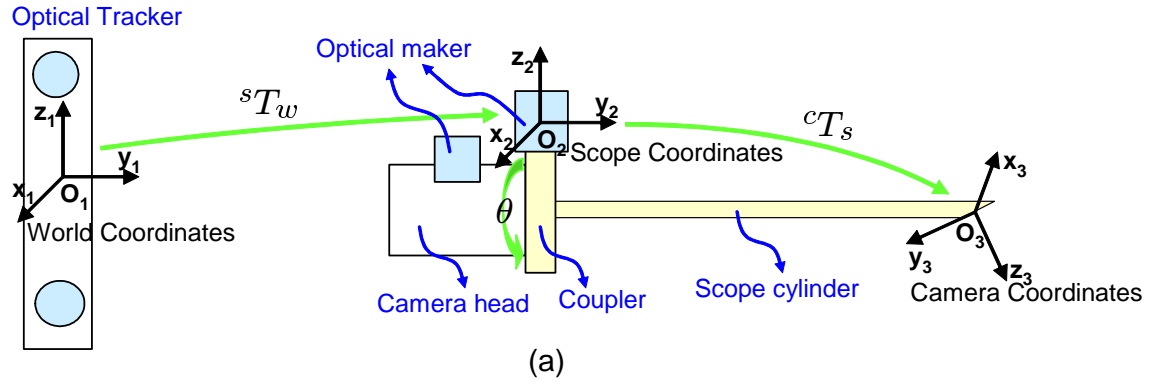


Figure 2: The geometric model of endoscope based on a tracking system. A new coupler (see Fig. 1 (b)) is designed to mount an optical marker to the scope cylinder which ensures that the transformation from scope(marker) coordinates O_2 to the lens system (camera) coordinates O_3 is fixed. World coordinates O_1 is defined by the optical tracker. Two optical markers are attached to the coupler and camera head separately in order to compute the rotation θ in between.

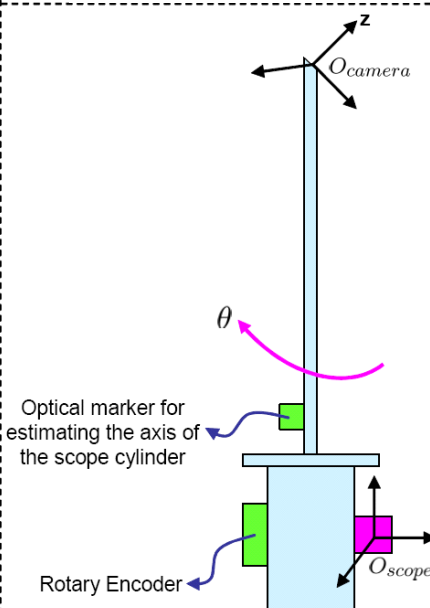
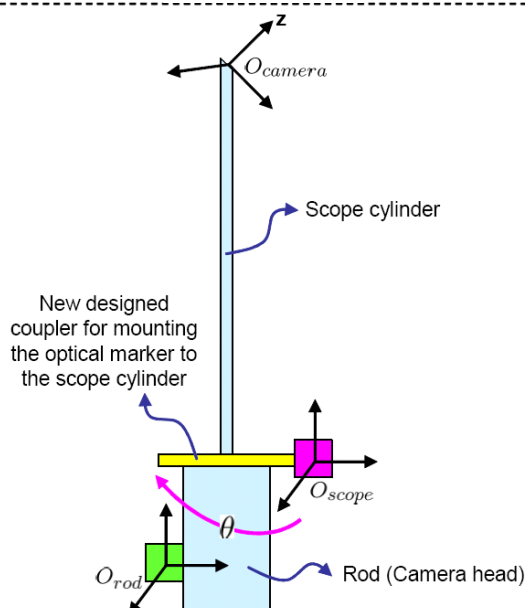
	Yamaguchi et al.'s system	Our system
System		
Reference part	Rod (Camera head)	Scope cylinder
Rotated part	Scope cylinder	Rod (Camera head)
Fact	<ol style="list-style-type: none"> 1. Lens system is rotated around the scope cylinder by θ 2. Image plane is fixed 	<ol style="list-style-type: none"> 1. Image plane is rotated around the principal point by θ 2. Lens system is fixed
Extra Transformation	<ol style="list-style-type: none"> 1. Rotate the scope cylinder around its axis by θ 2. Inversely rotate the image plane around z-axis of the lens system by θ 	<ol style="list-style-type: none"> 1. Rotate the image plane around the principal point by θ
Unknown parameters	<ol style="list-style-type: none"> 1. θ 2. Axis of the scope cylinder 3. Axis of the lens system 	<ol style="list-style-type: none"> 1. θ 2. Principal point

Figure 3: A comparison between Yamaguchi et al.'s system and ours. In Yamaguchi et al.'s system, the camera head is tracked such that the transformation from the marker to the lens system is not fixed but depends on the rotation angle θ . Let the marker coordinates as a reference, the lens system is rotated around the scope cylinder about θ , but the image plane (that is in the camera head) remains the same. They use two additional transformation to describe the effect of rotation, so their model becomes complicated. Moreover, they need to calibrate the axis of both the scope cylinder and the lens system by using another optical maker attached to the scope cylinder. Based on our observation, it is possible to simplify the model if we fix the transformation between the marker and the lens system. We design a coupler that enables the mounting of the optical marker onto the scope cylinder. Then we set the marker coordinates as a reference, the lens system is fixed. The rotation only affects the image plane since the camera head is rotated around the cylinder (reference). And the image plane only rotates around the principal point. Since the principal point is an intrinsic parameter, we only need to estimate the rotation angle. As a result, we come up with a very simple model (see details in the text).

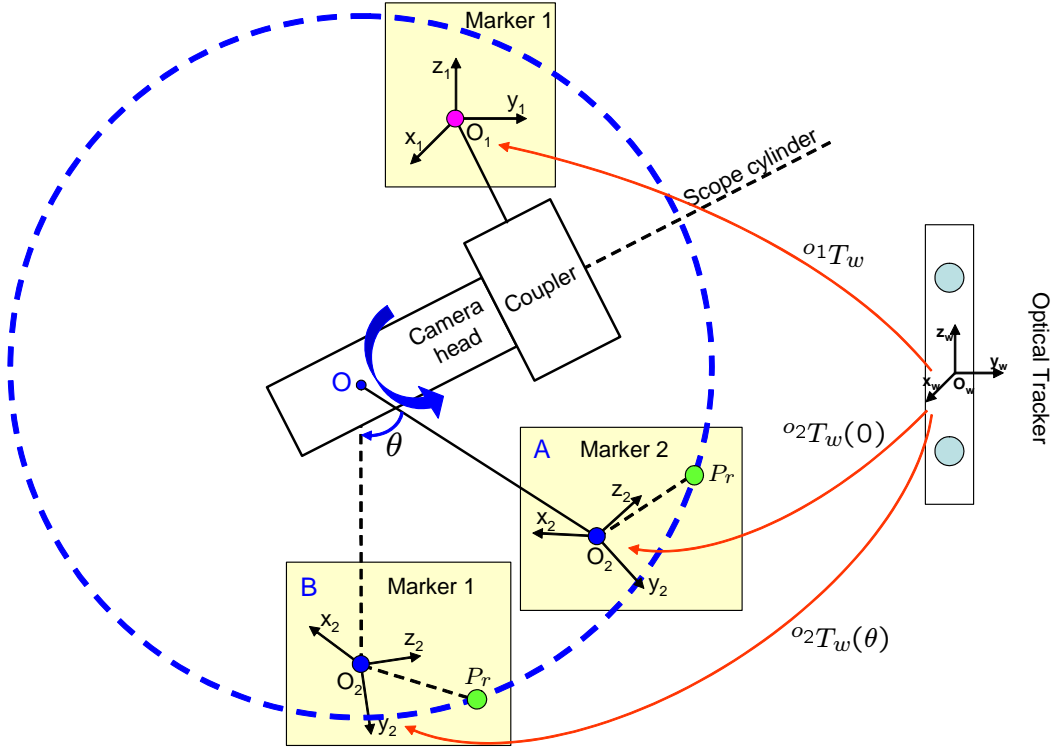


Figure 4: Illustration of the relationship between the rotation angle θ and two marker coordinates. (O_1 is attached to the scope cylinder and O_2 is attached to the camera head. A indicates the position of O_2 when $\theta = 0$ and B indicates the position of O_2 given a rotation θ . Given any point P_r in O_2 , its trace with the rotation of the camera head is a circle in Marker 1's coordinates O_1 . It moves from position P_i^A to P_i^B in Marker 1's coordinates O_1 . This circle is also on the plane perpendicular to the axis of scope cylinder. O is the center of the circle.

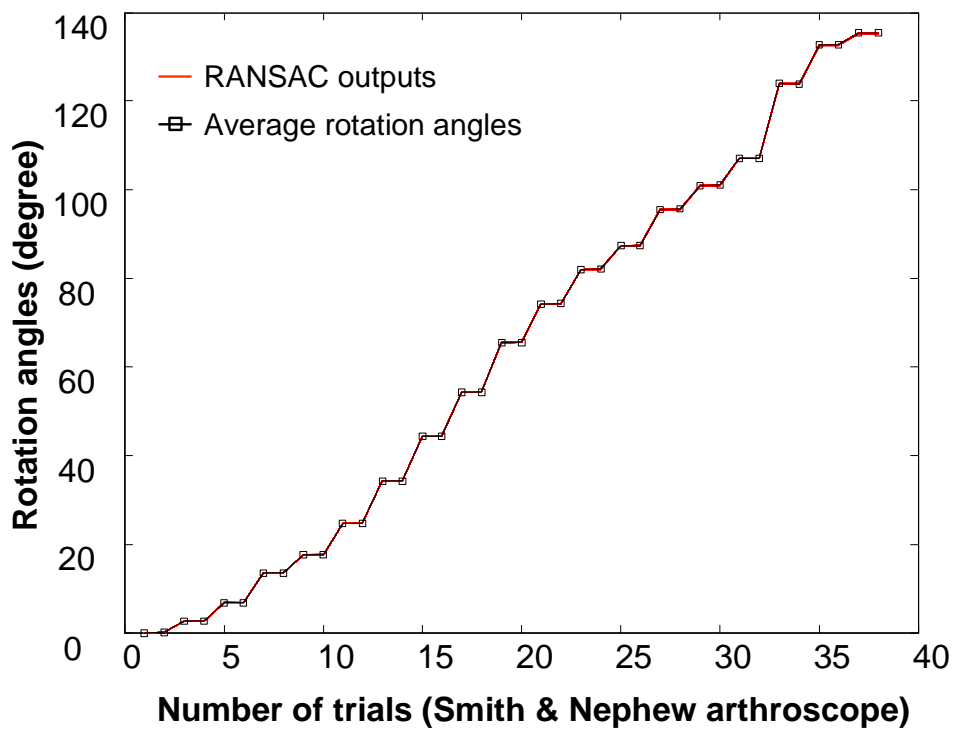
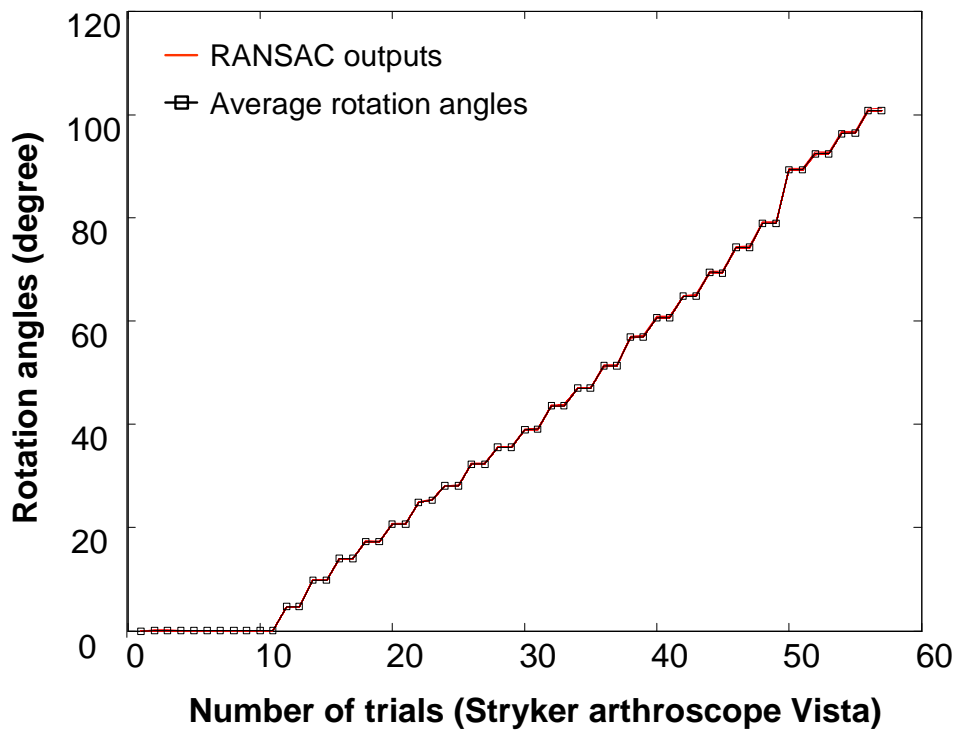


Figure 5: Estimated rotation angles for two endoscopes. In each trial we rotated the camera head with respect to the scope cylinder and captured an image. We captured a few images for the initial position. After that we took two images for each rotation angle. The red curves are estimated rotation angles from different RANSAC iterations. The black curve is the average rotation angle. (Please enlarge the figure to see the difference between closely matching curves.)

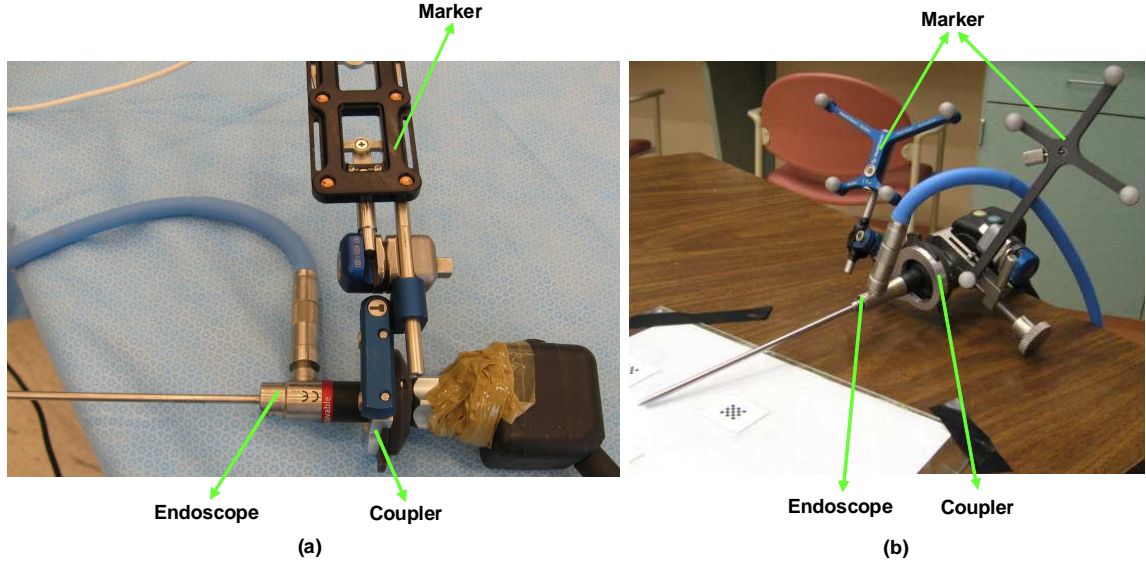


Figure 6: Endoscopes used in the experiments. (a) Smith & Nephew video arthroscope - autoclavable SN-OH 272589 (30 degree, 4mm). (b) Stryker 344-71 arthroscope Vista (70 degree, 4mm).

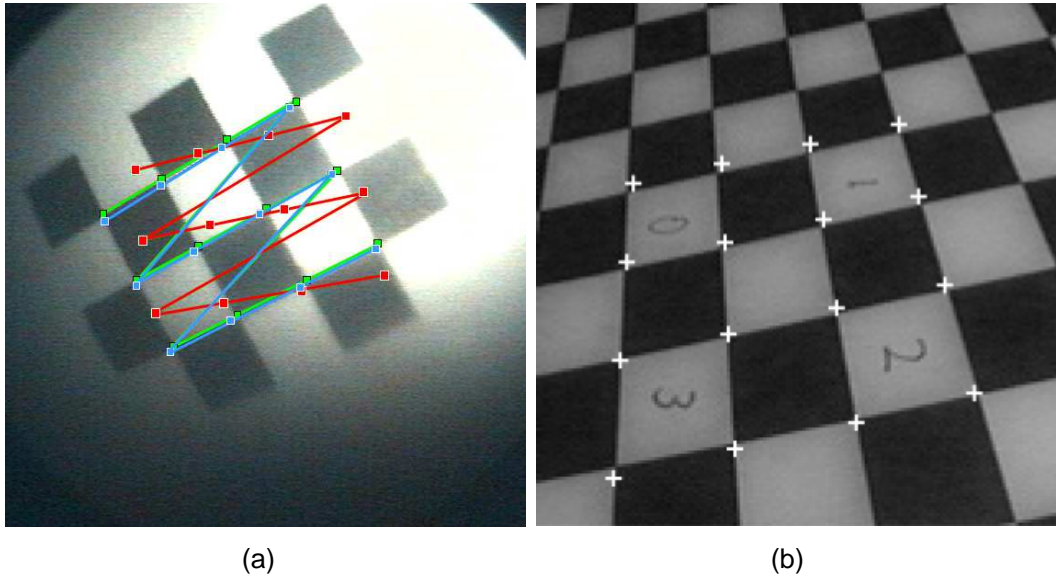


Figure 7: (a) Illustration of the back projection with and without a rotation compensation. Green points are ground truth - 2D corner pixels on the image of the calibration pattern. Red points are back projection of the 3D world positions of the corners using the first equation of Eq. 2, which has no rotation compensation. Blue points are back projection using both equations of Eq. 2. Since the rotation is included in the camera model, the back projected pixels are much closer to the ground truth than the red points. (b) An image used in Yamaguchi et al. [11, 12]’s paper. This image has a higher resolution, better lighting and less distortion than ours.

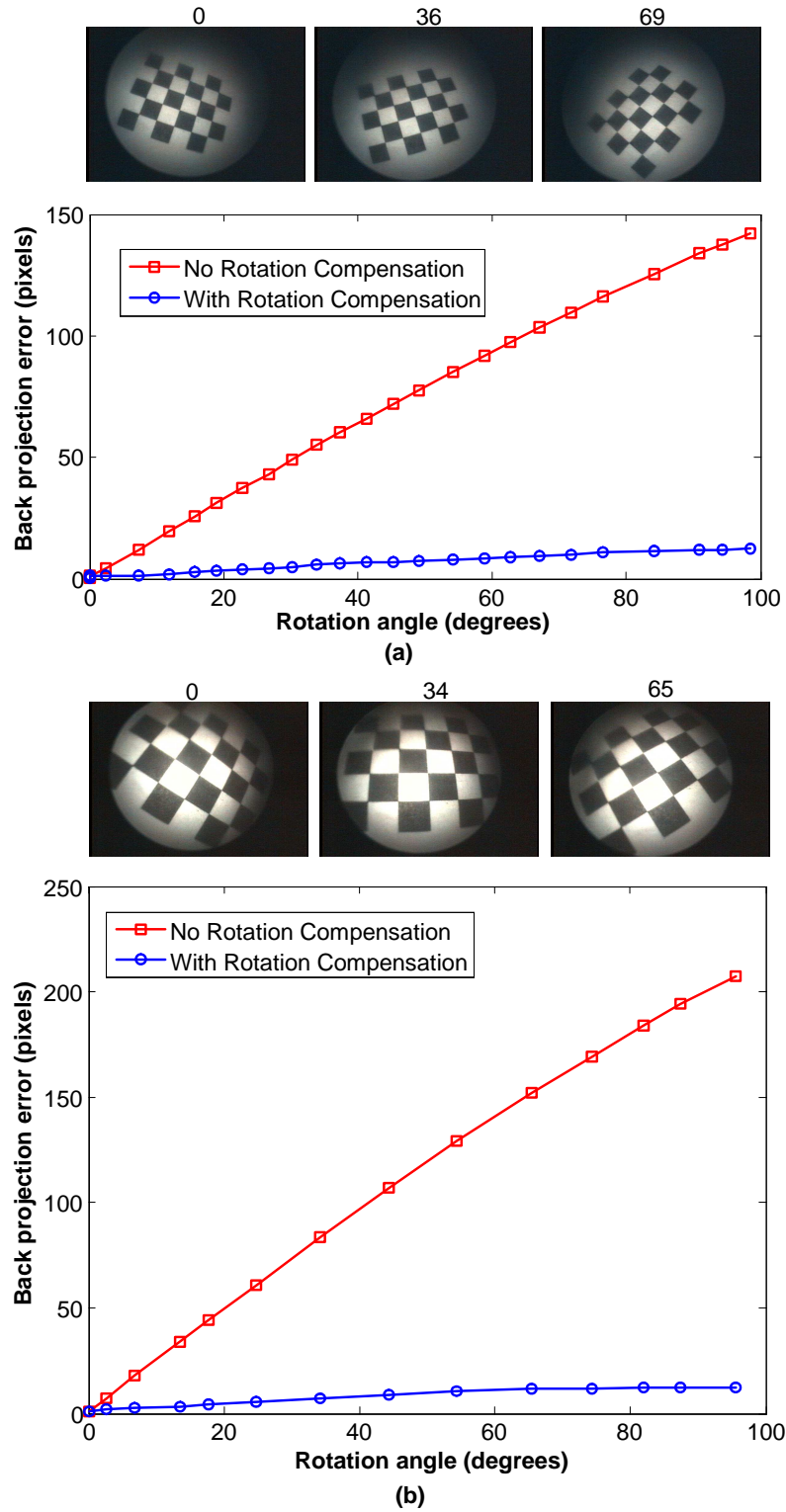


Figure 8: Back projection errors with respect to the rotation angles for two systems. (a) Stryker 344-71 arthroscope Vista and Polaris optical tracker in our lab. (b) Smith & Nephew video arthroscope and OPTOTRAK optical tracker in the operating room. Images in the top row of (a) and (b) correspond to different rotation angles (the number is shown on the top of each image). The red curves in (a) and (b) represent the errors without a rotation compensation. The blue curves in (a) and (b) are errors with a rotation compensation.

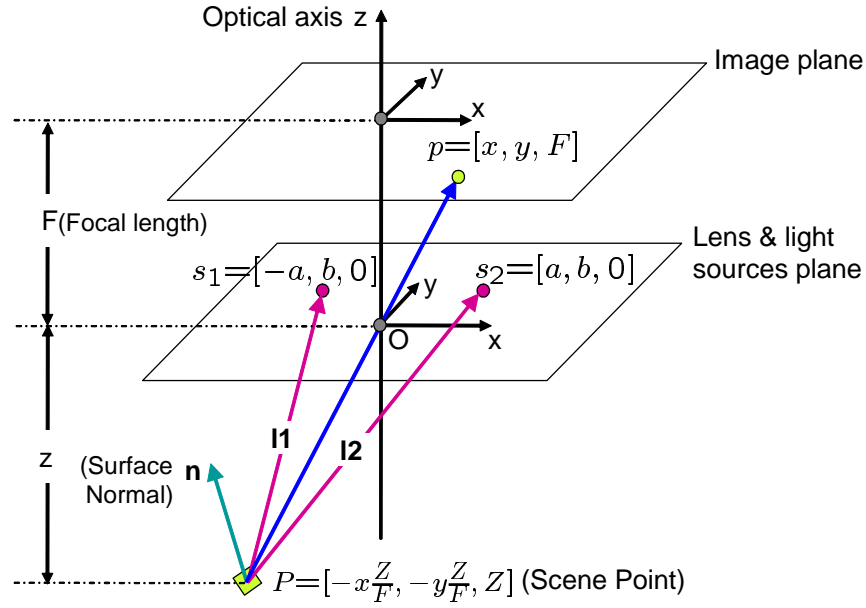


Figure 9: Illustration of the perspective projection model for endoscope imaging system with two near point light sources: O is the camera projection center. s_1 and s_2 indicate two light sources. We assume the plane consisting of O , s_1 and s_2 is parallel to the image plane. The coordinates system is centered at O and Z is parallel to the optical axis, and pointing toward the image plane. X and Y are parallel to the image plane. F is the focal length. a and b are two parameters related to the position of the light sources. Given a scene point P , the corresponding image pixel is p . Assuming a Lambertian surface, the surface illumination therefore depends on the surface albedo, light source intensity and fall off, and the angle between the normal and light rays.

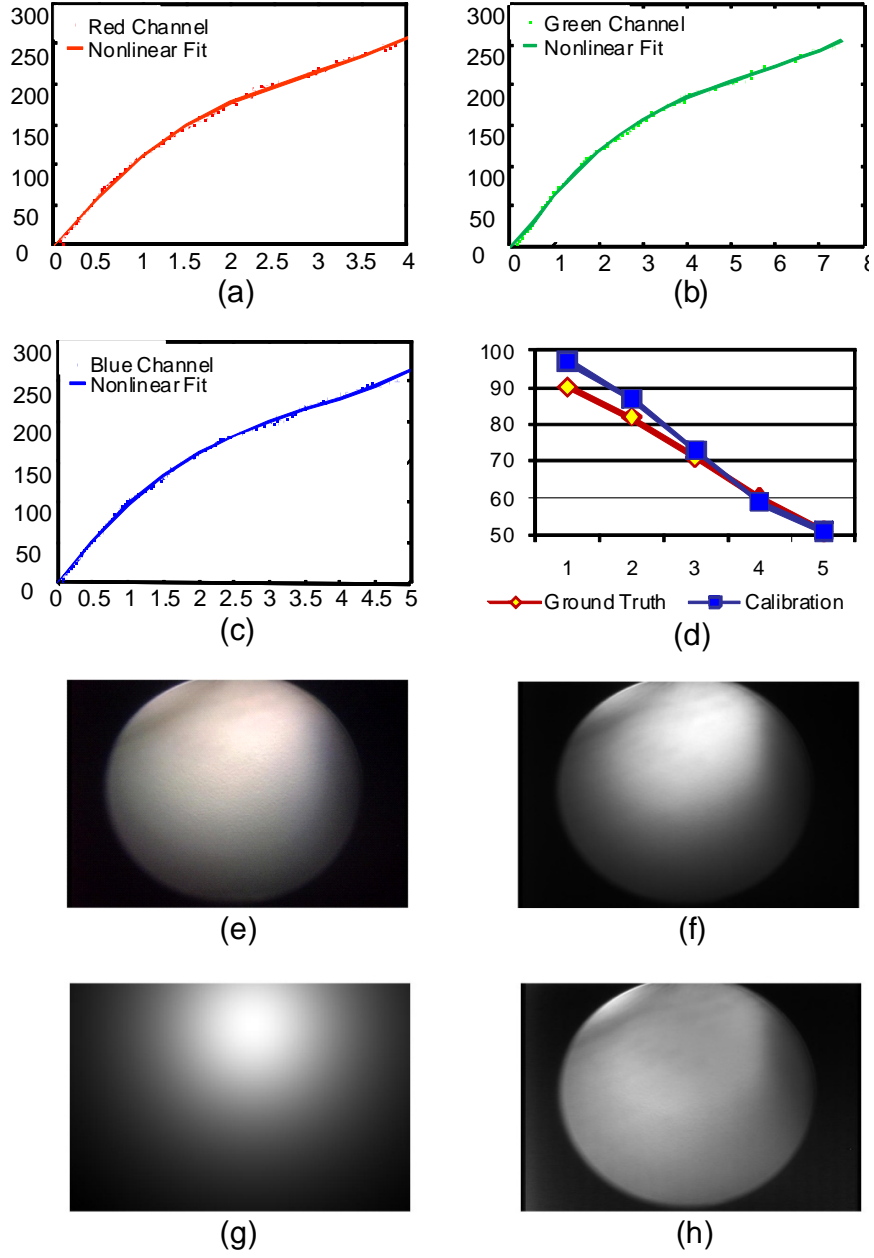


Figure 10: Results of photometric calibration. (a) camera response function in Red channel. Red dots represents the data points and magenta line represents the nonlinear fit. (b) camera response function in Green channel. Green dots represents the data points and magenta line represents the nonlinear fit. (c) camera response function in Blue channel. Blue dots represents the data points and magenta line represents the nonlinear fit. (d) Calibrated light intensity in different level (blue) and ground truth (green). We use level 6 as a reference and plot level 1-5 with small level corresponding to high light intensity. A bit variation in range of the high intensities may be caused by saturation. (e) Original image of color chart. (f) \tilde{m} . (g) the cosine term $\frac{(n) \cdot l_1}{r_1^2} + \frac{(n) \cdot l_2}{r_2^2}$. (h) the spacial distribution function $m(x, y)$.